Published in final edited form as:

Eur Radiol. 2018 January ; 28(1): 124–132. doi:10.1007/s00330-017-4925-6.

Statistical Clustering of Parametric Maps from Dynamic Contrast Enhanced MRI and an Associated Decision Tree Model for Non-Invasive Tumour Grading of T1b Solid Clear Cell Renal Cell Carcinoma

Yin Xi[1], **Qing Yuan**[1], **Yue Zhang**[1], **Ananth J. Madhuranthakam**[1,2], **Michael Fulkerson**[1], **Vitaly Margulis**[3,4], **James Brugarolas**[4,5], **Payal Kapur**[3,4,6], **Jeffrey A. Cadeddu**[3,4], and **Ivan Pedrosa**[1,2,4]

[1]Department of Radiology, UT Southwestern Medical Center, 2201 Inwood Road, Dallas, TX

[2]Advanced Imaging Research Center, UT Southwestern Medical Center, 2201 Inwood Road, Dallas, TX

[3]Department of Urology, UT Southwestern Medical Center, 2201 Inwood Road, Dallas, TX

[4]Kidney Cancer Program, Simmons Comprehensive Cancer Center, UT Southwestern Medical Center, 2201 Inwood Road, Dallas, TX

[5]Department of Internal Medicine, UT Southwestern Medical Center, 2201 Inwood Road, Dallas, TX

[6]Department of Pathology, UT Southwestern Medical Center, 2201 Inwood Road, Dallas, Texas, USA

Abstract

Corresponding Author: Ivan Pedrosa, MD, Department of Radiology. UT Southwestern Medical Center, 2201 Inwood Road. Dallas, TX 75235-9085, (Phone) 214-645-2285, (Fax) 214-645-2762, Ivan.Pedrosa@UTSouthwestern.edu.

Compliance with ethical standards:

Ethical approval:

Institutional Review Board approval was obtained.

Informed consent:

Written informed consent was obtained from all subjects (patients) in this study.

Guarantor:

The scientific guarantor of this publication is Ivan Pedrosa.

Conflict of interest:

The authors of this manuscript declare no relationships with any companies, whose products or services may be related to the subject matter of the article.

Statistics and biometry:

One of the authors has significant statistical expertise.

Study subjects or cohorts overlap:

Some study subjects or cohorts have been previously reported in Yuan, Q., et al., *Intratumor Heterogeneity of Perfusion and Diffusion in Clear-Cell Renal Cell Carcinoma: Correlation With Tumor Cellularity.* Clin Genitourin Cancer, 2016. 14(6): p. e585–e594.T1b

Methodology:

- prospective
- cross sectional study / observational
- performed at one institution

Objectives—To apply a statistical clustering algorithm to combine information from dynamic contrast enhanced (DCE) magnetic resonance imaging (MRI) into a single tumour map to distinguish high- (HG) from low-grade (LG) T1b clear cell renal cell carcinoma (ccRCC).

Methods—This prospective, IRB-approved, HIPAA-compliant study included 18 patients with solid T1b ccRCC who underwent pre-surgical DCE MRI. After statistical clustering of the parametric maps of K^{trans}, K_{ep} and iAUC with a fuzzy c-means (FCM) algorithm, each tumour was segmented into three regions (low/medium/high active areas). Percentages of each region and tumour size were compared to tumour grade at histopathology. A decision tree model was constructed to select the best parameter(s) to predict HG ccRCC.

Results—Seven HG and 11 LG T1b ccRCCs were included. HG histology was associated with higher percent high active areas ($p = 0.0154$) and this was the only feature selected by the decision tree model, which had a diagnostic performance of 78% accuracy, 86% sensitivity, 73% specificity, 67% PPV, and 89% NPV.

Conclusions—The FCM integrates multiple DCE-derived parameter maps and identifies tumour regions with unique pharmacokinetic characteristics. Using this approach, a decision tree model using criteria beyond size to predict tumour grade in T1b ccRCCs is proposed.

Keywords

Kidney cancer; Clear-cell renal cell carcinoma; Dynamic contrast enhanced-MRI; tumour heterogeneity; statistical clustering

INTRODUCTION

Kidney cancer is the tenth most common cancer in humans with an estimated 62,700 new cases and 14,240 deaths in the U.S. in 2016[1]. More than 90% of kidney cancers are renal cell carcinomas (RCC) and about 70% of these are clear cell RCC (ccRCC)[1]. The serendipitous discovery of RCC has been steadily increasing with the proliferation of cross-sectional imaging studies[2]. However, the resulted increased detection on early stages has not translated into reduction of cancer-specific mortality possibly indicating the over-treatment of small, potentially indolent renal tumours[3]. Consequently, active surveillance (AS) has become an acceptable option for the management of patients with incidentally discovered small renal masses (i.e. T1a disease)[4]. Although the risk of developing metastases for these patients is small, it increases in larger and high grade tumours[5]. Similarly, ccRCC carries a worse prognosis than other pathologic subtypes with lower prevalence such as papillary and chromophobe RCC[6]. The association between clear cell histology and worse prognosis has not been specifically documented for T1b tumours although a higher tumour grade is associated with worse disease free-survival in these tumours[7]. Furthermore, while the safety of AS in T1b RCC has been reported[8], the reliability of tumour biopsies to accurately grade RCC may be limited in larger, heterogeneous tumours and its role in providing an accurate histologic subtype and nuclear grade may be limited[9,10]. The lack of reliable predictors of oncologic behaviour represent an important argument for resistance to using AS, particularly in patients with larger, heterogeneous renal masses (T1b disease)[8,11]. An imaging biomarker could help overcome this limitation by offering complementary information about tumour

biology/aggressiveness in the whole tumour in patients with larger (T1b), heterogeneous, biopsy-confirmed ccRCCs.

Multiphasic contrast-enhanced magnetic resonance imaging (MRI) can help in the characterization of RCC subtypes based on the degree of enhancement[12–14]. Alternatively, a high temporal resolution dynamic contrast enhanced (DCE) MRI approach combined with pharmacokinetic modelling of signal intensity allows for quantitative assessment of tumour vascularity with extraction of parameters such as the transfer constant between the intravascular and extravascular space (K^{trans}), the rate constant (K_{ep}), and the fractional volume of the extravascular extracellular (Ve) and vascular (Vp) space[15–19]. Efforts to correlate DCE MRI-derived pharmacokinetic parameters to tumour grade in RCC have offered variable results to date[16,20]. Furthermore, the integration of large amounts of data generated in quantitative model-based pharmacokinetic maps challenges the applicability of tumour characterization with DCE MRI in clinical practice. Moreover, it is unclear if such-model based quantitative parameters offer additional information compared to other simpler semi-quantitative measures based on enhancement changes (e.g. initial area under the concentration curve [$iAUC$]). Clustering algorithms such as fuzzy c-means (FCM) of DCE-MRI data has been proved to be a useful tool in segmenting tissues in kidney[21] and to characterize and assess treatment response in heterogeneous tumours in the breast[22,23] and brain[24]. To our knowledge, the value of pattern recognition techniques based on FCM algorithms to distinguish RCC grades has not been reported.

The purpose of this preliminary study was to apply a statistical clustering algorithm to combine information from multiple quantitative pharmacokinetic maps derived from DCE MRI to generate a single tumour map for the diagnosis of high-grade T1b clear cell renal cell carcinoma.

MATERIAL AND METHODS

PATIENT POPULATION

This was an Institutional Review Board approved Health Insurance Portability and Accountability Act-compliant prospective study. Inclusion criteria: 1) patients with a known renal mass confined to the kidney that is >4 cm but ≤7 cm in size, 2) scheduled for surgical resection, 3) agreed to undergo a research MRI prior to surgery, and 4) histopathological confirmation of clear cell histology with pathologic stage T1b after nephrectomy. All patients signed an informed consent prior to the MRI examination. Exclusion criteria: 1) patients with predominantly cystic masses on MRI (i.e. more than 75 % of the mass demonstrating non-enhancing fluid signal with a thin wall), 2) contraindication for MRI (e.g. MRI unsafe indwelling devices), 3) pregnancy, 4) renal function impairment (estimated glomerular filtration rate [eGFR] <30 mL/min/1.73 m^2), and 5) unable to complete the MRI examination (e.g. claustrophobia). Seventy-eight consecutive patients with known renal masses were recruited between August 2012 and August 2014. Among those, 54 patients completed the MRI examination and had a diagnosis of ccRCC at pathology after surgery. Nine of those 54 were predominantly cystic ccRCCs and therefore excluded. Of the remaining 45, 18 were T1b ccRCCs. As a result, 18 patients with solid T1b tumours were included and represent our study population (Figure 1). Data from DCE MRI acquisitions in

18 of these patients was previously reported but the analysis and results of the data of the previous report do not overlap with this analysis[25].

MAGNETIC RESONANCE IMAGING PROTOCOL

All patients underwent MRI on 3T dual-transmit MRI scanner with phased-array torso coils (Achieva and Ingenia, Philips Healthcare, Best, The Netherlands) before surgery (average MRI-surgery time = 4 ± 3 days). A multiparametric MRI protocol included T2-weighted imaging for anatomic localization with the following imaging parameters: echo time (TE)/ repetition time (TR) = 80/1115 ms, flip angle (FA) = 90°, number of signal averages (NSA) = 1, field of view (FOV) = 402×340 mm^2, acquisition matrix = 284×268, bandwidth = 467 Hz per pixel. DCE MRI was performed using a coronal three-dimensional (3D) spoiled gradient echo (SPGR) sequence before, during, and after the administration of a bolus of 0.1 mmol/kg body weight of gadobutrol (Gadavist; Bayer Healthcare Pharmaceuticals, Wayne, NJ) at a rate of 2 mL/s followed by a 20 mL saline flush at 2 mL/s. A slightly slower injection rate than previously reported was used to compensate for the lower temporal resolution of the 3D acquisition and the high flow rate anticipated in the kidney and ccRCC. DCE images were acquired for about 6 minutes at a 5-second per dynamic phase with the following parameters: TR/TE = 3/1.53 ms, FA = 10°, NSA = 1, slice thickness = 5 mm, FOV = 180 × 408 mm^2, acquisition matrix =120 × 288, bandwidth = 1326 Hz per pixel. To minimize respiratory motion, 3 consecutive dynamic phases (5 seconds each) were obtained within each 15-second breath-held acquisition period with a 15-second period of free-breathing between consecutive acquisition periods. Prior to the DCE acquisition 3 coronal SPGR acquisitions with the same image parameters as those described above but with flip angles of 2, 5, and 10 degrees respectively, were obtained for the purpose of calculating tissue T1 relaxation[25].

IMAGE ANALYSIS

Only DCE MRI data were included for the purpose of this study. DCE images were analysed with a commercial software, VersaVue Enterprise (iCAD Inc, Nashua, NH) with voxel by voxel fitting of the change of contrast agent concentration in tumour using the extended Tofts model. Quantitative maps of K^{trans} and K_{ep} were generated after motion correction using a non-rigid registration algorithm in VersaVue software[26] in 18 patients. A population-based arterial input function (AIF)[27] was used since the temporal resolution of the 3D DCE acquisition used in this study precluded the accurate measurement of individual AIF. The initial area under the concentration curve ($iAUC$) was calculated during 60 seconds after contrast arrival[28,29].

All DCE images and parametric maps were analysed using the open-source Picture Archiving and Communications System (PACS) viewer (Osirix X, version 5.6, 64-bit, Bernex, Switzerland). A representative slice location through the centre of the mass was selected by a radiologist (I.P., more than 15 years of experience) who was unaware of the final pathology. Regions of interest (ROIs) were drawn by the same radiologist to outline the periphery of the target lesion. Pixel-by-pixel values of K^{trans}, K_{ep} and $iAUC$ of the tumour ROI were exported for fuzzy c-means clustering analysis. The maximum dimension in the cranio-caudal direction (SL), latero-lateral direction (LL) and anterior-posterior direction

(SP) was recorded. Three tumour size measurements on each renal mass were made: 1) maximum length ($Length_{max}$) of the tumour (cm) in the anterio-posterior (AP), latero-lateral (LL), or supero-inferior (SI) dimension; 2) tumour area within a region of interest (ROI) drawn to outline the periphery of the renal mass ($Area_{roi}$); and 3) estimated tumour volume (Vol_{est}) as SI × LL × AP. Further, we generated a surrogate of tumour shape by calculating the standard deviation of the lengths from AP, SI and LL. A round shaped tumour would have similar dimensions in all three orthogonal planes thus having a small shape measurement. An elliptical tumour would have a larger shape measurement since the differences among the dimensions were larger.

FUZZY C-MEANS CLUSTERING

Pixels within the tumour ROI in the representative slices from all patients were exported together and used for clustering (see below). Their DCE-derived parameters, K^{trans}, K_{ep} and iAUC, were recorded. All values were logarithmically transformed to correct for right skewness. Due to positive correlation between DCE-derived parameters, three clusters were used to classify different regions. They were named as low-active area (LAA), medium-active area (MAA) and high-active area (HAA). A Fuzzy c-means (FCM) algorithm was then applied to the parameter domain with the number of clusters set at three[30]. The initial cluster centres were set such that the centre for LAA had lower K^{trans}, lower K_{ep} and lower iAUC (i.e. 25th percentile in the population); the centre for MAA had intermediate K^{trans}, intermediate K_{ep} and intermediate iAUC (i.e. median); and the centre for HAA had highest K^{trans}, highest K_{ep} and highest iAUC (i.e. 75th percentile for HAA). The FCM algorithm recursively calculates between two steps until the objective function is minimized: step 1) calculate the membership to each data point corresponding to each cluster centre based on distance between the cluster centre and the data point; and step 2) calculate the cluster centres as the weighted summation of the data points where the membership was used as weights. The objective function is the weighted summation of the distances between all points and all cluster centres with the membership as the weight. For each point, its membership to each of the three clusters are represented by three numbers between 0 and 1. These numbers can also be interpreted as the probability of belonging to each of the clusters. Therefore, the summation of the three memberships should be one for each point. After the objective function is minimized, each point is assigned to the cluster with the highest membership. The assigned cluster labels are then mapped back to the tumour ROIs.

HISTOPATHOLOGICAL ANALYSIS

Histopathologic results after surgical resection of the tumour served as the reference standard in all cases. The final diagnosis was provided by an uropathologist (more than 10 years of experience). All tumours were classified based on the International Society of Urological Pathology (ISUP) grading system as low-grade ccRCC (LG ccRCC; ISUP I–II) or high-grade ccRCC (HG ccRCC; ISUP III–IV). The presence of necrosis at histopathology was recorded.

STATISTICAL ANALYSIS

First, the percentages of LAA, MAA and HAA in each tumour were calculated (noted as %LAA, %MAA and %HAA). Second, the differences in the median of each tumour

percentage area as well as the tumour size measurements between HG and LG ccRCCs were tested using Wilcoxon rank sum test univariately. The presence of necrosis at histopathology was also compared to tumour size and percentage areas.

Third, using tumour histopathology as reference, a binary decision tree model was constructed and tested to identify a strategy to best classify the tumours based on the variables calculated above[31]. Briefly, a binary decision tree model first ranks all variables according to their correlation to the reference (known as importance). The candidate variables included: 1) tumour size measurements ($Length_{max}$, $Area_{roi}$, Vol_{est} and shape); 2) tumour activity measurements from FCM (% LAA, % MAA and % HAA); and 3) tumour pharmacokinetic parameters (mean and standard deviation of K_{ep}, K^{trans} and $iAUC$). Then, the model selected a subset of the candidate variables and built a set of hierarchical rules that best discriminates HG and LG ccRCCs. Subsequently, the data is split into two sub-groups according to the variable with the highest importance and a cutoff that optimizes the overall accuracy (node). This procedure is repeated for each of the sub-groups until a minimum size is reached or no improvement can be made. The minimum size for terminal node was set to 5 to avoid overfitting. To minimize the bias created by training and validating the model using the same data, a leave-one-out cross-validation technique was implemented[32]. The purpose was to train the decision tree on all but one tumour in the dataset, and compare the prediction of the tumour that was “left out” to its final histopathology diagnosis. This routine was repeated for each tumour in the data set, and the sensitivity, specificity, positive and negative predictive values were calculated. 95% bootstrap confidence intervals were also calculated. A p value <0.05 was considered statistically significant. All statistical analyses were performed using the software, R (version 3.2.4, Vienna, Austria). The Rpart package was utilized for the construction of the decision tree model.

RESULTS

Eighteen patients (15 male, 3 female; mean age ± SD, 60 ± 8 years) were included in this study. Patients’ characteristics are shown in Table 1. Seven patients had HG and 11 patients had LG ccRCC. No significant difference was found in any of the size measurements between HG and LG ccRCCs (Table 2, Figure 2). There was no statistical difference in mean length between tumours without (5.4 ± 0.9 cm) and with necrosis (6.4 ± 0.7 cm, p>0.05).

Fuzzy C-Means clustering

A total of 22192 pixels were collected from all tumours. Pearson correlation coefficients were 0.75 between K_{ep} and iAUC, 0.77 between K^{trans} and iAUC, and 0.88 between K^{trans}, K_{ep}, which indicated strong positive correlation (i.e. pixels with higher K^{trans} would also had higher K_{ep} and higher iAUC). The fuzzy C-means algorithm performed as expected with pixels from HAA exhibiting the highest values in all three DCE parameters while pixels from LAA showed the lowest (Table 3). Representative parametric and fuzzy c-means maps are shown in Figure 3.

Median and mean ± standard deviation of percentage areas were 5.6% and 8.9% ± 8.8% (HG) and 34.0% and 30.1% ± 17.9% (LG) for %LAA, 42.8% and 40.1% ± 16.6% (HG) and 37.7% and 40.2% ± 13.9% (LG) for %MAA, and 53.6% and 51.1% ± 20.6% (HG) and

19.6% and 29.8% ± 22.5% (LG) for %HAA. Figure 5 gives a visual representation of the distributions of the percentage areas for HG and LG tumours. Wilcoxon rank sum test showed statistical significant differences in the median percent areas between HG and LG ccRCC in %LAA and %HAA but not %MAA (p value = 0.02 (LAA), 0.72 (MAA) and 0.02 (HAA)).

Decision Tree Model

The optimal decision tree model was constructed with selection of only one of the candidate variables, %HAA. According to the model, tumours were classified as LG when %HAA < 27% and HG when %HAA was ≥27%. An example in Figure 4 illustrates how %HAA helps predicting tumour grade.

After leave-one-out cross-validation, the accuracy, sensitivity, specificity, positive and negative predictive value (PPV, NPV) for the diagnosis of HG ccRCC were estimated as 78% (50%, 100%), 86% (66%, 100%), 73% (58%, 100%), 67% (56%, 100%) and 89% (63%, 100%).

DISCUSSION

The implementation of active surveillance (AS) protocols for the management of small renal masses is based on the presumption that the risk of metastatic disease is minimal and likely lower than the morbidity and mortality associated with surgical and/or ablative interventions ([33–35]). To minimize the risk of metastasis in AS patients, most would advocate for tumour subtyping and grading with percutaneous biopsy at the time of diagnosis to rule out high grade disease. However, this approach is not without limitations as serious complications associated to percutaneous biopsies occur in approximately 2–4% of patients[36,37]. Importantly, incorrect tumour grading on percutaneous biopsies may occur in up to 30% of the renal masses sampled[37] and likely more common in larger, heterogeneous tumours. The inability to accurately grade the latter (i.e. T1b renal masses) is an obstacle towards implementation of AS in patients with larger tumours despite evidence indicating that AS for many of these may be indeed safe[8]. This is particularly relevant in the case of clear cell histology given its association with worse prognosis and the inherent tumour heterogeneity that characterizes this disease[38]. Our preliminary results suggest that a dynamic contrast enhanced magnetic resonance imaging (DCE-MRI) protocol may add valuable information to the pre-surgical characterization of T1b ccRCC.

Traditionally, the presence of intratumoural heterogeneity within a given tumour is not integrated into the analysis of imaging examinations performed for characterization of renal masses although the overall imaging phenotype is known to correlate with the final histopathologic diagnosis[39]. However, the subjective nature of image interpretation leads to unreliable results because of differences in training, experience, and other possible factors affecting decision-making. To maximize the utility of the acquired imaging data, statistical analyses such as histograms, probability distributions, spatial analyses, and clustering have been introduced to quantify tumour heterogeneity and help improve diagnoses[40–44]. Our study introduces a novel approach by combining three DCE MRI-derived parameters to draw a simplified map of tumour vascular heterogeneity in ccRCC. The FCM algorithm

offers a possibility to summarize multiple DCE-derived pharmacokinetic maps and identify unique tumour regions with different enhancement characteristics.

Tumour size measurements were not helpful in differentiating HG from LG ccRCCs in our study. This is consistent with previous reports illustrating the association between age, sex, and size with increased risk of malignancy but moderate diagnostic performance of preoperative tools (e.g. nomograms) based on these variables for the prediction of tumour grade[45]. Our proposed decision tree model had an overall accuracy, sensitivity, specificity, positive and negative predictive value (PPV, NPV) for the diagnosis of HG ccRCC of 78%, 86%, 73%, 67% and 89%, respectively. These preliminary results, if validated in larger series, could have immediate clinical applicability in patients with inconclusive tumour grading (e.g. scant tissue) on percutaneous biopsy and those where the biopsy may be challenging based on the tumour location. Based on its high negative predictive value (89%), DCE MRI may serve as a complementary test to percutaneous biopsy when selecting patients with heterogeneous T1b renal masses for AS. Moreover, the statistical association between the percentage of HAA and HG histology suggests that directing percutaneous biopsies to those areas of the tumour with HAA could yield a higher diagnostic performance for the detection of its more aggressive component. Prior reports have demonstrated an ability of different MRI techniques such as arterial spin labelled perfusion, DCE MRI, and diffusion weighted imaging to detect intratumoural heterogeneity of microvessel density and tumour cellularity[15,46].

Implementation of the proposed DCE MRI protocol as a screening method with the potential to replace percutaneous biopsy to identifying high-grade ccRCC would require a high sensitivity and NPV. In our cohort, with cross-validation adjustment, the overall sensitivity and NPV of the resulting tree were 86% and 89%, respectively. Thus, 11% of tumours classified as LG would be misclassified. While encouraging, these results would indicate that percutaneous biopsy is still preferable in most clinical scenarios. However, with further refinements of this model (e.g. whole tumour assessment) it could potentially replace the percutaneous biopsy in carefully selected clinical scenarios such as in patients with other comorbidities, and those with difficult access and/or inherent increased risk of complications.

Our study has several limitations. First, although we have pathologic confirmation in all cases a correlation between tumour heterogeneity on DCE MRI and at histopathology was not performed. In addition, because of the small sample size we did not have any grade 4 RCCs. Second, our information on tumour vascularity was limited to K^{trans}, K_{ep} and iAUC. We did not include other parametric variables such as Ve and Vp into our study due to their high noise level. Third, the FCM algorithm provides information about each pixel behaviour during the DCE-MRI experiment but it does not take into account information about the location of the pixels. For this reason, we were not able to quantify spatial heterogeneity patterns similar to those in previous reports[43,44]. Fourth, the confidence interval of the diagnostic performance was wide due to small sample size. Thus, the generalizability of this method needs to be tested on a larger dataset. Finally, we only analysed a single slice location through the centre of the mass for each of the DCE parametric maps. Analysis of multiple slices covering the entire renal mass may enhance the assessment of tumour

heterogeneity. We chose a single slice analysis based on the practicality of implementing this type of analysis in routine clinical practice. While expansion from 2-D to 3-D statistical models deserves further investigation, we anticipate that implementation of the latter would be more challenging (i.e. need to draw multiple ROIs per tumour and substantial increase in computation power needs).

In conclusion, the application of the fuzzy c-means method to the DCE MRI data could facilitate the implementation of DCE MRI protocols in clinical practice by offering a single map that can be generated in seconds and be easily analyse in the context of an MRI exam performed for evaluation of a renal mass. The proposed statistical method offers an objective, quantitative analysis with the potential to offer meaningful information about the tumour biology in patients. Using this approach, we were able to construct a decision tree model to predict tumour grade in T1b renal masses. Further validation of our preliminary results with this novel statistical method in larger patient cohorts is needed.

Acknowledgments

Funding:

This study has received funding by the NIH grants #P50CA196516 and #5RO1CA154475.

REFERENCE LIST

1. Society, AC. Cancer Facts and Figures 2016. 2016. <http://www.cancer.org/research/cancerfactsstatistics/cancerfactsfigures2016/>
2. Chow WH, Devesa SS, Warren JL, Fraumeni JF Jr. Rising incidence of renal cell cancer in the United States. Jama. 1999; 281:1628–1631. [PubMed: 10235157]
3. Cooperberg MR, et al. Decreasing size at diagnosis of stage 1 renal cell carcinoma: analysis from the National Cancer Data Base, 1993 to 2004. J Urol. 2008; 179:2131–2135. DOI: 10.1016/j.juro.2008.01.097 [PubMed: 18423754]
4. Campbell SC, et al. Guideline for management of the clinical T1 renal mass. J Urol. 2009; 182:1271–1279. DOI: 10.1016/j.juro.2009.07.004 [PubMed: 19683266]
5. Abel EJ, et al. Identifying the risk of disease progression after surgery for localized renal cell carcinoma. BJU Int. 2010; 106:1277–1283. DOI: 10.1111/j.1464-410X.2010.09337.x [PubMed: 20394619]
6. Teloken PE, et al. Prognostic impact of histological subtype on surgically treated localized renal cell carcinoma. J Urol. 2009; 182:2132–2136. DOI: 10.1016/j.juro.2009.07.019 [PubMed: 19758615]
7. Igarashi T, et al. The impact of a 4 cm. cutoff point for stratification of T1N0M0 renal cell carcinoma after radical nephrectomy. J Urol. 2001; 165:1103–1106. [PubMed: 11257647]
8. Mehrazin R, et al. Growth kinetics and short-term outcomes of cT1b nd cT2 renal masses under active surveillance. J Urol. 2014; 192:659–664. DOI: 10.1016/j.juro.2014.03.038 [PubMed: 24641909]
9. Dechet CB, et al. Prospective analysis of computerized tomography and needle biopsy with permanent sectioning to determine the nature of solid renal masses in adults. J Urol. 2003; 169:71–74. DOI: 10.1097/01.ju.0000042211.18318.ba [PubMed: 12478106]
10. Lebret T, et al. Percutaneous core biopsy for renal masses: indications, accuracy and results. J Urol. 2007; 178:1184–1188. discussion 1188. DOI: 10.1016/j.juro.2007.05.155 [PubMed: 17698122]
11. Sun M, et al. Treatment management of small renal masses in the 21st century: a paradigm shift. Ann Surg Oncol. 2012; 19:2380–2387. DOI: 10.1245/s10434-012-2247-0 [PubMed: 22322956]

12. Sun MR, et al. Renal cell carcinoma: dynamic contrast-enhanced MR imaging for differentiation of tumor subtypes--correlation with pathologic findings. Radiology. 2009; 250:793–802. DOI: 10.1148/radiol.2503080995 [PubMed: 19244046]
13. Chandarana H, et al. Histogram analysis of whole-lesion enhancement in differentiating clear cell from papillary subtype of renal cell cancer. Radiology. 2012; 265:790–798. DOI: 10.1148/radiol.12111281 [PubMed: 23175544]
14. Notohamiprodjo M, et al. Combined diffusion-weighted, blood oxygen level-dependent, and dynamic contrast-enhanced MRI for characterization and differentiation of renal cell carcinoma. Acad Radiol. 2013; 20:685–693. DOI: 10.1016/j.acra.2013.01.015 [PubMed: 23664397]
15. Zhang Y, et al. Tumor Vascularity in Renal Masses: Correlation of Arterial Spin-Labeled and Dynamic Contrast-Enhanced Magnetic Resonance Imaging Assessments. Clin Genitourin Cancer. 2016; 14:e25–36. DOI: 10.1016/j.clgc.2015.08.007 [PubMed: 26422014]
16. Chandarana H, et al. High temporal resolution 3D gadolinium-enhanced dynamic MR imaging of renal tumors with pharmacokinetic modeling: preliminary observations. J Magn Reson Imaging. 2013; 38:802–808. DOI: 10.1002/jmri.24035 [PubMed: 23389833]
17. Wu WC, Su MY, Chang CC, Tseng WY, Liu KL. Renal perfusion 3-T MR imaging: a comparative study of arterial spin labeling and dynamic contrast-enhanced techniques. Radiology. 2011; 261:845–853. DOI: 10.1148/radiol.11110668 [PubMed: 22095996]
18. Notohamiprodjo M, et al. Measuring perfusion and permeability in renal cell carcinoma with dynamic contrast-enhanced MRI: a pilot study. J Magn Reson Imaging. 2010; 31:490–501. DOI: 10.1002/jmri.22028 [PubMed: 20099364]
19. Abdel Razek AA, Mousa A, Farouk A, Nabil N. Assessment of Semiquantitative Parameters of Dynamic Contrast-Enhanced Perfusion MR Imaging in Differentiation of Subtypes of Renal Cell Carcinoma. Pol J Radiol. 2016; 81:90–94. DOI: 10.12659/PJR.894707 [PubMed: 27026793]
20. Cornelis F, et al. Multiparametric magnetic resonance imaging for the differentiation of low and high grade clear cell renal carcinoma. European radiology. 2015; 25:24–31. DOI: 10.1007/s00330-014-3380-x [PubMed: 25117747]
21. Yang X, et al. Nonrigid Registration and Classification of the Kidneys in 3D Dynamic Contrast Enhanced (DCE) MR Images. Proc SPIE Int Soc Opt Eng. 2012; 8314:83140B.
22. Chang YC, et al. Classification of breast mass lesions using model-based analysis of the characteristic kinetic curve derived from fuzzy c-means clustering. Magn Reson Imaging. 2012; 30:312–322. DOI: 10.1016/j.mri.2011.12.002 [PubMed: 22245697]
23. Shi J, et al. Treatment response assessment of breast masses on dynamic contrast-enhanced magnetic resonance scans using fuzzy c-means clustering and level set segmentation. Med Phys. 2009; 36:5052–5063. DOI: 10.1118/1.3238101 [PubMed: 19994516]
24. Farjam R, Tsien CI, Lawrence TS, Cao Y. DCE-MRI defined subvolumes of a brain metastatic lesion by principle component analysis and fuzzy-c-means clustering for response assessment of radiation therapy. Med Phys. 2014; 41:011708. [PubMed: 24387500]
25. Fram EK, et al. Rapid calculation of T1 using variable flip angle gradient refocused imaging. Magn Reson Imaging. 1987; 5:201–208. [PubMed: 3626789]
26. Periaswamy S, Farid H. Elastic registration in the presence of intensity variations. Ieee T Med Imaging. 2003; 22:865–874. DOI: 10.1109/Tmi.2003.815069
27. Parker GJ, et al. Experimentally-derived functional form for a population-averaged high-temporal-resolution arterial input function for dynamic contrast-enhanced MRI. Magn Reson Med. 2006; 56:993–1000. DOI: 10.1002/mrm.21066 [PubMed: 17036301]
28. Evelhoch JL. Key factors in the acquisition of contrast kinetic data for oncology. J Magn Reson Imaging. 1999; 10:254–259. [PubMed: 10508284]
29. O'Connor JPB, Jackson A, Parker GJM, Roberts C, Jayson GC. Dynamic contrast-enhanced MRI in clinical trials of antivascular therapies. Nat Rev Clin Oncol. 2012; 9:167–177. DOI: 10.1038/nrclinonc.2012.2 [PubMed: 22330689]
30. Bezdek, J. Pattern Recognition with Fuzzy Objective Function Algorithms. Springer US; 2012. C.
31. Breiman, L., F, JH., Olshen, RA., Stone, CJ. Classification and Regression Trees. Wadsworth: 1984.

32. Efron B. Jackknife, Bootstrap and Other Resampling Methods in Regression-Analysis - Discussion. Ann Stat. 1986; 14:1301–1304. DOI: 10.1214/aos/1176350145
33. Stephenson AJ, Hakimi AA, Snyder ME, Russo P. Complications of radical and partial nephrectomy in a large contemporary cohort. J Urol. 2004; 171:130–134. DOI: 10.1097/01.ju.0000101281.04634.13 [PubMed: 14665860]
34. Uzzo RG, Novick AC. Nephron sparing surgery for renal tumors: indications, techniques and outcomes. J Urol. 2001; 166:6–18. [PubMed: 11435813]
35. Volpe A, et al. Contemporary management of small renal masses. Eur Urol. 2011; 60:501–515. DOI: 10.1016/j.eururo.2011.05.044 [PubMed: 21664040]
36. Mally AD, Gayed B, Averch T, Davies B. The current role of percutaneous biopsy of renal masses. Can J Urol. 2012; 19:6243–6249. [PubMed: 22704306]
37. Phe V, Yates DR, Renard-Penna R, Cussenot O, Roupret M. Is there a contemporary role for percutaneous needle biopsy in the era of small renal masses? BJU Int. 2012; 109:867–872. DOI: 10.1111/j.1464-410X.2011.10544.x [PubMed: 21895938]
38. Gerlinger M, et al. Intratumor heterogeneity and branched evolution revealed by multiregion sequencing. N Engl J Med. 2012; 366:883–892. DOI: 10.1056/NEJMoa1113205 [PubMed: 22397650]
39. Pedrosa I, et al. MR classification of renal masses with pathologic correlation. Eur Radiol. 2008; 18:365–375. [PubMed: 17899106]
40. Yang X, Knopp MV. Quantifying Tumor Vascular Heterogeneity with Dynamic Contrast-Enhanced Magnetic Resonance Imaging: A Review. Journal of Biomedicine and Biotechnology. 2011; 2011:12.
41. Sinha S, et al. Multifeature analysis of Gd-enhanced MR images of breast lesions. J Magn Reson Imaging. 1997; 7:1016–1026. [PubMed: 9400844]
42. Chen W, Giger ML, Li H, Bick U, Newstead GM. Volumetric texture analysis of breast lesions on contrast-enhanced magnetic resonance images. Magn Reson Med. 2007; 58:562–571. [PubMed: 17763361]
43. O'Sullivan F, Roy S, Eary J. A statistical measure of tissue heterogeneity with application to 3D PET sarcoma data. Biostatistics. 2003; 4:433–448. [PubMed: 12925510]
44. O'Sullivan F, Roy S, O'Sullivan J, Vernon C, Eary J. Incorporation of tumor shape into an assessment of spatial heterogeneity for human sarcomas imaged with FDG-PET. Biostatistics. 2005; 6:293–301. [PubMed: 15772107]
45. Shin TY, et al. Assessing the anatomical characteristics of renal masses has a limited effect on the prediction of pathological outcomes in solid, enhancing, small renal masses: results using the PADUA classification system. BJU Int. 2014; 113:754–761. DOI: 10.1111/bju.12446 [PubMed: 24053790]
46. Yuan Q, et al. Intratumor Heterogeneity of Perfusion and Diffusion in Clear-Cell Renal Cell Carcinoma: Correlation With Tumor Cellularity. Clin Genitourin Cancer. 2016

ABBREVIATIONS AND ACRONYMS

RCC	Renal Cell Carcinoma
ccRCC	Clear-Cell Renal Cell Carcinoma
AS	Active Surveillance
HG/LG	High Grade/Low Grade
DCE-MRI	Dynamic Contrast-Enhanced Magnetic Resonance Imaging
K^{trans}	Transfer Constant between the Intravascular and Extravascular Extracellular Space

K_{ep}	Rate Constant
Ve	Fractional Volume of the Extravascular Extracellular Space
Vp	Fractional Plasma Volume
iAUC	Initial Area Under the Concentration Curve
SPGR	spoiled gradient echo
PACS	Picture Archiving and Communications System
ROI	Region of Interest
SI	Superior to Interior
LL	Lateral to Lateral
AP	Anterior to Posterior
$\mathbf{Length_{max}}$	maximum length
$\mathbf{Area_{ROI}}$	tumour area within a region of interest drawn to outline the periphery of the renal mass
$\mathbf{Vol_{est}}$	estimated tumour volume
FCM	Fuzzy C-means
ISUP	International Society of Urological Pathology
LAA	Low Active Area
MAA	Medium Active Area
HAA	High Active Area
%LAA	Percent Low Active Area
%MAA	Percent Medium Active Area
%HAA	Percent High Active Area
PPV	Positive Predictive Value
NPV	Negative Predictive Value
FOV	field of view
FA	flip angle
NSA	number of signal average
TE	echo time
TR	repetition time

KEY POINTS

1. Tumour size did not correlate with tumour grade in T1b clear-cell RCC.
2. Tumour heterogeneity can be analysed using statistical clustering via DCE-MRI parameters.
3. High grade ccRCC has a larger percentage of high active area than low grade ccRCCs.
4. A decision tree model offers a simple way to differentiate HG/LG ccRCCs

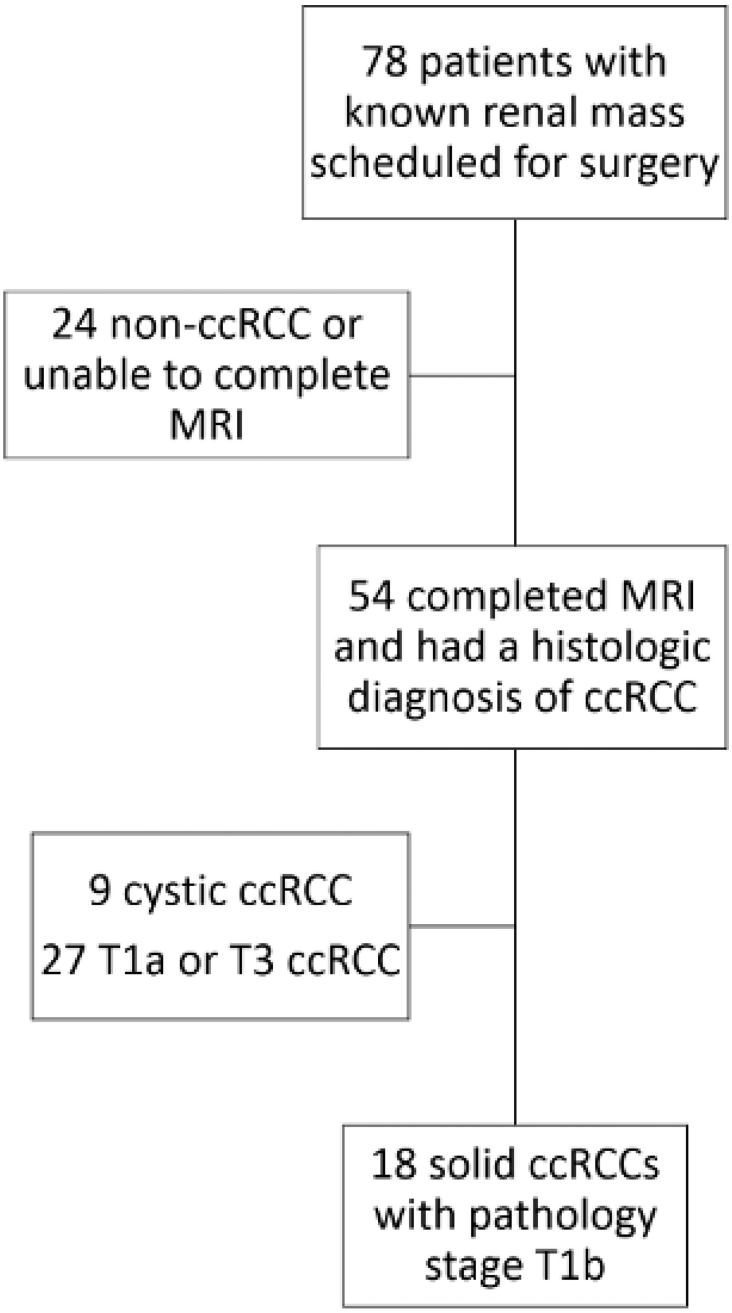

Figure 1.
Diagram of the flow of participation. ccRCC= clear cell renal cell carcinoma

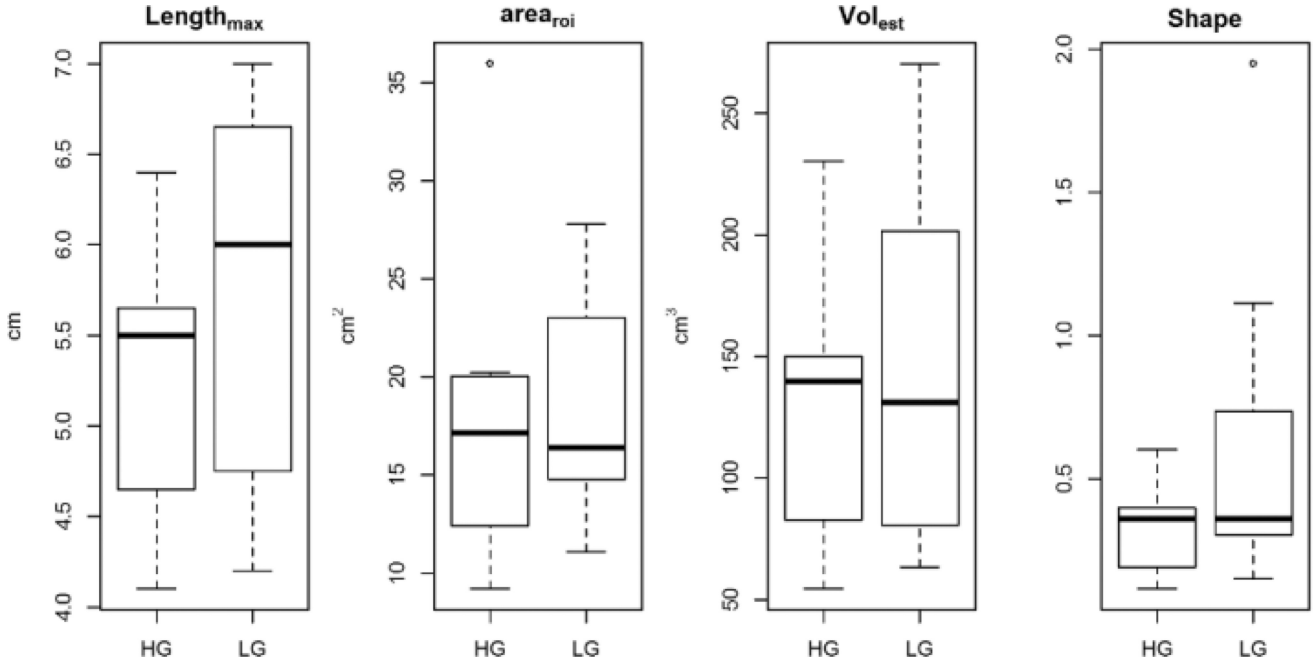

Figure 2.

Box-plots of $Length_{max}$, $Area_{roi}$, Vol_{est} and shape in HG and LG ccRCCs. No significant difference was found in any of these size measurements (all P values > 0.05).

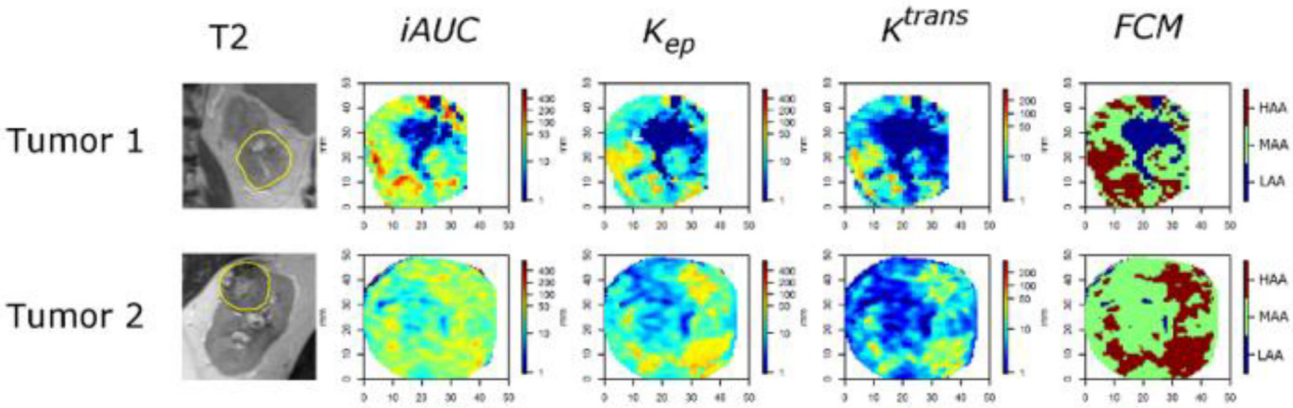

Figure 3.

MRI in 2 ccRCCs. From left: T2-W; DCE maps (*iAUC, K_{ep}, K^{trans}*); and FCM. *iAUC* dominated the FCM result in tumour 1. In tumour 2, *iAUC* did not show particular pattern of heterogeneity while islands of high enhancement were visible in K_{ep} and K^{trans}. Both tumour 1 and tumour 2 are HG.

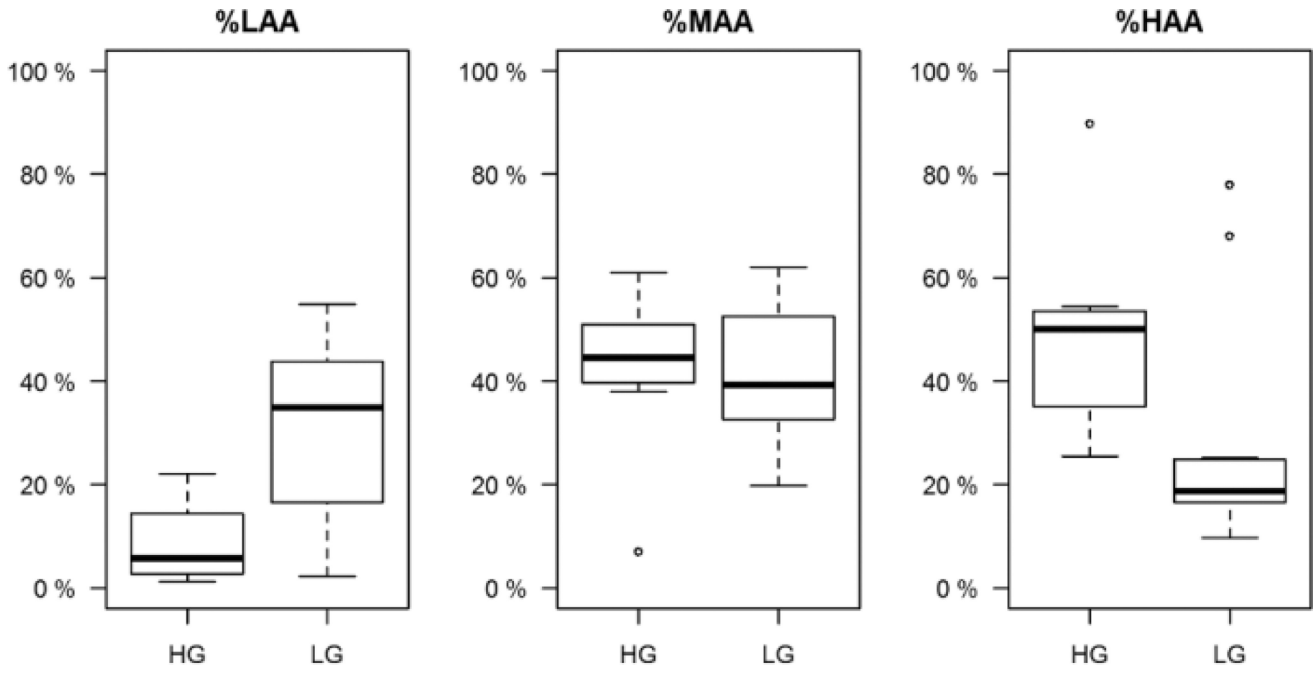

Figure 4.

Boxplots of percent areas for HG and LG ccRCCs. %LAA: percent low-active-area; %MAA: percent-medium-active-area; %HAA: percent high-active-area. Significant difference in median was observed in %LAA and %HAA between HG and LG ccRCC but not in %MAA (p value = 0.02 (LAA), 0.72 (MAA) and 0.02 (HAA)).

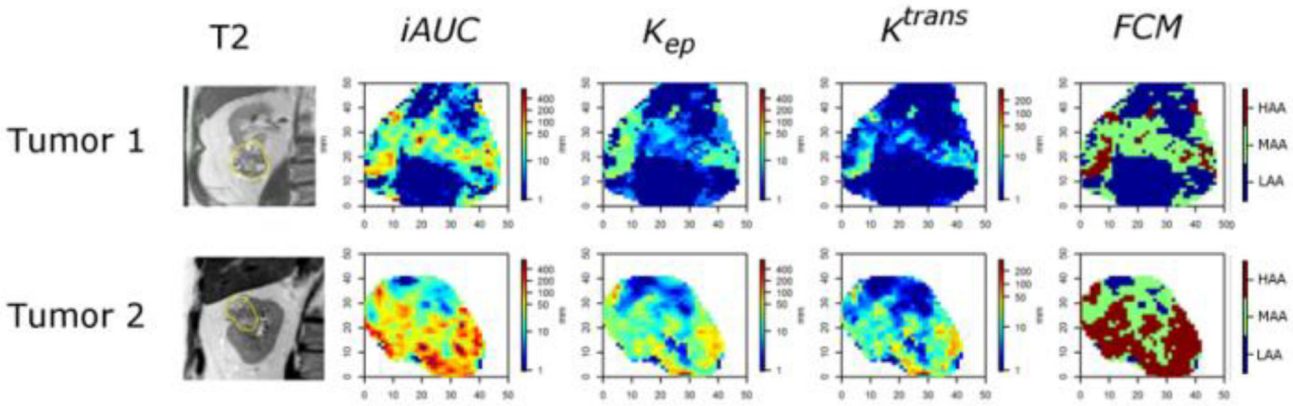

Figure 5.

Characterization of T1b RCCs. Representative examples illustrating the contribution of %HAA to classify T1b RCCs into HG and LG ccRCC based on the decision tree model. From left: T2-W; DCE maps (iAUC, Kep, Ktrans); and FCM. Tumour 1 is larger (Lengthmax = 6.5 cm) but has lower %HAA (10%, maroon on FCM) than Tumour 2 (Lengthmax = 4.8 cm), which has a high %HAA (55%, maroon on FCM). The decision tree predicted low-grade histology for tumour 1 and high grade for tumour 2, respectively. Histopathologic analysis confirmed the results of the decision tree model with clear cell renal cell carcinoma ISUP grade II and III for Tumour 1 and 2, respectively.

Table 1

Patient characteristics.

Characteristic	No. of Patients	%
Age (years)	60±8	
Gender		
M	15	83.3
F	3	16.7
T Stage		
Ib	18	100
ISUP Grade		
I	0	0
II	11	61.1
III	7	38.9
IV	0	0
Necrosis		
Yes	3	16.7
No	15	83.3
Treatment		
RPN	12	66.7
LRN	5	27.8
OPN	1	5.6

Data in cells represent mean values ± standard deviation.

ISUP= International Society of Urological Pathology. RPN= Robotic partial nephrectomy. LRN= Laparoscopic radical nephrectomy. OPN= open partial nephrectomy.

Table 2

Median and Mean ± Standard Deviation of Tumour Size Measurements

	All ccRCCs		HG ccRCCs		LG ccRCCs		P value for Wilcoxon rank sum test
	Median	Mean ± SD	Median	Mean ± SD	Median	Mean ± SD	
$Length_{max}$	5.7 cm	5.5 ± 1 cm	5.5 cm	5.2 ± 0.8 cm	6 cm	5.7 ± 1 cm	0.2
$Area_{roi}$	17 cm^2	18 ± 7 cm^2	17 cm^2	18 ± 9 cm^2	16.4 cm^2	19 ± 6 cm^2	0.6
Vol_{est}	135 cm^3	137 ± 69 cm^3	140 cm^3	127 ± 61 cm^3	131 cm^3	144 ± 76 cm^3	0.7
Shape (SD of AP, SI and LL)	0.4	0.5 ± 0.4	0.36	0.3 ± 0.2	0.36	0.6 ± 0.5	0.2

Median and Mean ± standard deviation of maximum length ($Length_{max}$), area within the ROI ($Area_{roi}$), estimated tumour volume (Volest) and tumour shape (standard deviation of AP, SI and LL). Values were stratified by subtypes as well as for all tumours. Wilcoxon rank sum test was performed to test the difference in mean between HG and LG ccRCCs.

Table 3

Mean and standard deviation of *iAUC*, K_{ep} and K^{trans}.

	Number of pixels	*iAUC* (mm·sec)	K_{ep} (min^{-1})	K^{trans}(min^{-1})
Low-active area (LAA)	4291	1.3 ± 3	0.5 ± 2	0.11 ± 0.5
Medium-active area (MAA)	10333	25.6 ± 39	11.0 ± 7	4.1 ± 3
High-active area (HAA)	7569	87.4 ± 109	35.9 ± 27	19.2 ± 17

Mean and standard deviation of *iAUC*, K_{ep} and K^{trans} stratified by active areas for all tumour pixels combined. High-active area had the highest values in all three DCE parameters while low-active area had the lowest values.